

Integration of Sentinel-1 and Sentinel-2 data for change detection: A case study in a war conflict area of Mosul city

Falah Fakhri ^{a,*}, Ioannis Gkanatsios ^b

^a Independent Non-Profitable Researcher, Turku, Finland

^b Data Scientist, Astrosat, Edinburgh, United Kingdom



ARTICLE INFO

Keywords:

Synthetic aperture radar (SAR)

Change detection

Machine learning

SVM

Sentinel-1

Sentinel-2

ABSTRACT

The city of Mosul located approximately 400 km North of Baghdad was captured by the Islamic State during the period 04th – 06th of June in 2014. The impact of conflict had devastated results on buildings and the infra-structure of the city.

Remote sensing technology has proven an extremely useful tool for monitoring changes. In this study, a combination of Synthetic Aperture Radar (SAR) and optical imagery is used to map and monitor changes in the urban environment due to war.

In total, twenty of both Sentinel-1 and Sentinel-2 images were collected during the period of 2015 and 2019. The data were pre-processed and integrated to develop a supervised machine learning classification approach using Support Vector Machine (SVM) classifier. Texture analysis such as Grey Level Co-occurrence Matrix (GLCM) was also performed and combined with the other datasets.

Spectral indices have been used to improve the classification results such as: Band Ratio Built up Area (BRBA), New Built-up Area (BUI), Dry Bare Soil Index (DBSI), Modified Normalized Difference Water Index (MNDWI), Normalized Difference Vegetation Index (NDVI), and Soil Adjusted Vegetation Index (SAVI) which were derived from the optical data (Sentinel-2) to serve as an input to the classification scheme. The built-up area index was found to be one of the most important features in the classification scheme.

Results: show an overall accuracy of approximately 96% was achieved for all the scenes between 2015 and 2019. The change detection results show that the largest devastation occurred between 2017 and 2018 where the urban area was decreased by 427.65 km², where in 2019 the impact of the Mosul city was the lowest with a 296.8 km² urban loss. The developed approach showed an effectiveness in mapping the areas where conflict had the strongest impact.

1. Introduction

Remote sensing has become increasingly popular in the field of humanitarian action, because it is an independent and reliable source of information and allows both a quick response to emergencies and the monitoring of gradual changes. The coordination of humanitarian relief in natural disaster or a conflict situation, is often complicated by a scarcity of data to inform planning. Remote sensing imagery can give important insights in such conditions. Applications include situation awareness after natural disasters, structural damage assessment in conflict, monitoring human rights violations or population estimation in settlements (Lang et al., 2015; Quinn et al., 2017).

This is of importance when observations in the field area are not

possible because of limited budget, legal restrictions, or security reasons (Suriyaprasit and Shrestha, 2008; Fahnestock et al., 2016). Observation of specific places from space is not only crucial for decision making involving cases of humanitarian response to natural disasters or emergencies (Stow et al., 2015; Van Westen and C.J., 2013), but it also helps to develop a better general understanding of an area and how trends and temporal dynamics have shaped the spatial patterns of the present (Verbesselt et al., 2010; Gillanders et al., 2008). The investigation of combining and integrating SAR and optical datasets from different origins for an assessment of environmental conditions relevant to land use/land cover classes, are notably helpful in situations where dynamics arise from uncontrollable origins. (Braun and Hochschild, 2015).

Change detection (CD) analyses are known as useful methods in a

* Corresponding author.

E-mail address: falah.fakhri@outlook.com (F. Fakhri).

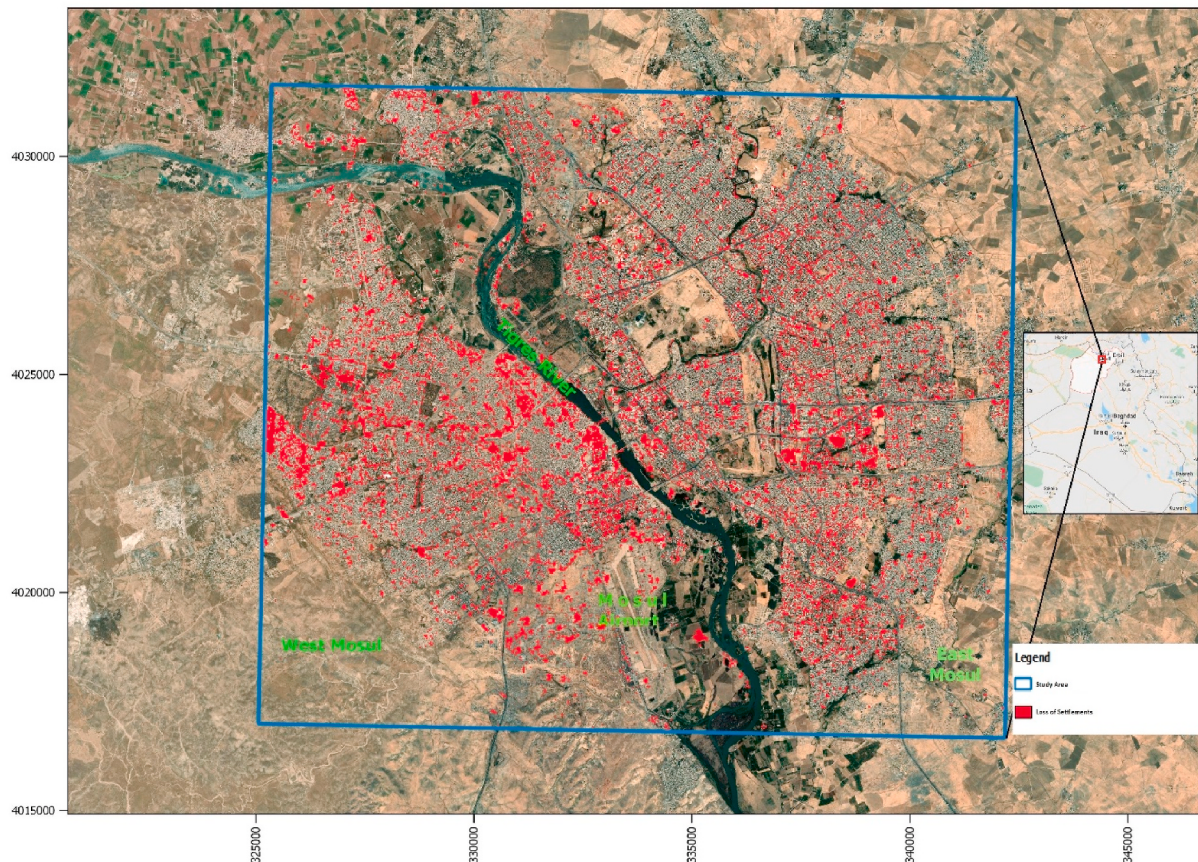


Fig. 1. Study area depicts on it the loss of settlements.

wide field of applications where differences of the state of the land are identified by observing them at different times. Change detection from remote sensing data is an incredibly challenging research problem, especially when we analyse an urban scene. Urban scenes are composed of many different types of objects, both natural and man-made. The urban landcover is complex to analyse as it exhibits many changes due to human activity and natural catastrophes. The need and necessity for tracking the changes in the built environment through time is essential for post-disaster recovery modelling, and remote sensing is particularly useful for obtaining this information when other sources of data are scarce or unavailable. Additionally, the longitudinal study of repeated observations over time in the built-up areas has its own complexities and limitations. Hence, a model is needed to overcome these barriers to extract the temporal variations from before to after the disaster event (Radke et al., 2005; Si Salah et al., 2019; Derakhshan et al., 2020).

Rapid, reliable, and continuous information is an essential component in disaster monitoring and management. CD methods have primarily been developed for imageries acquired from multispectral remote sensing platforms. The most widely used CD techniques in remote sensing are as follows: (1) post classification (Pilon et al., 1988; El-Hattab, 2016), (2) Principal Component Analysis (Fung and LeDrew, 1987), (3) Coherent change detection (Washaya et al., 2018) and (4) image differencing (Afify, 2011). Satellites carrying a multispectral sensor such as Landsat Thematic Mapper (TM) and more recently Sentinel-2 (S2) have been extensively used in change detection studies. However, the main limitation of these studies is the difficulty in acquiring cloud free images under cloudy and rainy weather conditions (Gillanders et al., 2008; Hansen et al., 2008). Hence, sometimes it becomes almost impossible to detect short- or long-term changes in an urban environment using time series optical dataset. Also, most of those studies employed pixel-based techniques which sometimes can be

insufficient for monitoring changes in a complex urban environment.

An alternative remote sensing sensor for collecting data from the surface of the Earth is the use of Synthetic Aperture Radar (SAR) that uses microwave radiation. Using SAR data for monitoring urban environments has some advantages over optical data. Microwaves can acquire data under any weather conditions (as they can penetrate through clouds). Also, SAR sensors could effectively detect changes on a built-up area based on the backscatter intensity of the radar signal. Another important consideration for using SAR rather than optical data is that the detection of changed targets in an urban setting should ignore seasonal variations such as vegetation phenology. The use of microwaves additionally increases the quality of the land cover assessments, as they allow a higher number of input images, especially in the rainy seasons. This helps to consider phenological variations of the images and reduces their potential bias impacting the results as the images are analysed as parts of a time series instead of a simple pre- and post-event change detection based on a single image pair (Pan et al., 2019; Braun et al., 2019). With the advent of globally available data with a satisfactory spatial resolution (20m) such as Sentinel-1 (S1), it allows for disaster monitoring anywhere on the world (Lefebvre, et al., 2016; Ma et al., 2016).

To date, only a few studies are found related to urban change monitoring due to anthropogenic disasters (Tapete et al., 2015; Washaya et al., 2018; Pan et al., 2018). All these studies employed SAR data to monitor urban changes over time. However, accurate classification of the urban environment using SAR data alone can be challenging. We propose a fresh perspective on urban change detection in a conflict zone using a combination of satellite sensors (SAR and optical) for classifying the urban environment and a post-classification technique to derive changes over time. This technique requires the comparison between two or more independently produced classified images.

Table 1

Synthetic aperture radar (SAR) and optical data used in this study.

Sentinel-1 (SLC)	Sentinel-1 (GRDH)	Orbit	Δt (days)	Sentinel-2
S1A_12/08/2015	S1A_12/08/2015	Descending	12	S2A_21/08/2015
S1A_24/08/2015	S1A_24/08/2015	Descending		
S1A_06/08/2016	S1A_06/08/2016	Descending	12	S2A_15/08/2016
S1A_18/08/2016	S1A_18/08/2016	Descending		
S1A_13/08/2017	S1A_13/08/2017	Descending	12	
S1A_25/08/2017	S1A_25/08/2017	Descending		S2A_30/08/2017
S1A_08/08/2018	S1A_08/08/2018	Descending	12	
S1A_20/08/2018	S1A_20/08/2018	Descending		S2B_20/08/2018
S1A_03/08/2019	S1A_15/08/2019	Descending		
S1A_15/08/2019	S1A_27/08/2019	Descending	12	S2B_25/08/2019

This has the advantage of not only deriving the distribution and size of the changed areas (positive and negative changes) but also minimizing the problem of normalizing for sensors and atmospheric differences between the image acquisitions.

This study aims to evaluate and monitor urban changes over time in a conflict zone in Mosul using an improved classification scheme to accurately classify the built-up area from the surroundings. To overcome some of the limitations of the other studies, this study attempts to (1) Develop a framework based on SAR (Sentinel-1) and optical (Sentinel-2) data, (2) Use a number of indices derived from Sentinel-2 data as well as texture analysis (Grey level Co-occurrence Matrix) for the classification scheme and (3) to maintain objectivity at the selection of reference areas even when field surveys are not possible because of limited budget and/or security concerns.

2. Materials and methods

2.1. Study area

Mosul is the capital of Ninawa province, a major city in northern Iraq. Located approximately 400 km north of Baghdad, Mosul stands on the west bank of the Tigris, opposite the ancient Assyrian city of Nineveh on the east bank (Fig. 1). The metropolitan area has grown to encompass substantial areas on both the “Left Bank” (east side) and the “Right Bank” (west side), as the two banks are described by the locals compared to the flow direction of Tigris. Islamic State in Iraq and Levant (ISIL) overran Mosul over the course of five days – 6–10 June 2014 – with little resistance from the Iraqi Army. The battle to recapture Mosul from ISIL began in October 2016 and lasted until July 2017 (Parker et al., 2014; Revkin and Jebari, 2019).

The United Nation (UN) has estimated that approximately 130,000 homes were destroyed during the battle and that the city is still littered with approximately 8 million tons of rubble and garbage, which could take up to 10 years to clean up (Danish Demining Group, 2019).

Revkin and Jebari (2019) indicated that the pace and visibility of reconstruction activities are indeed higher in east Mosul, compared to West Mosul as it was retaken several months later and sustained higher levels of damage.

To increase the potential of urban area monitoring and detecting the pre- and post-war conflict, both Sentinel-2 and Sentinel-1 data were selected, pre-processed and integrated to be used in the SVM classifier. Optical and radar remote sensing data are increasingly used for Land use \Land cover mapping and monitoring, their technical capabilities and tools are improving all the time and provide more accurate results (Niculescu et al., 2018; Tavares et al., 2019).

2.2. Data

As indicated in the previous studies and reports, the study area was subjected to rapidly devastation in short period. Hence, in order to take all these challenges into consideration, and prevent the deduction of false conclusions, SAR image pairs (S1) of Level-1 Single Look Complex (SLC) and Level-1 Ground Range Detected (GRD) were collected. In addition, optical data (S2) between 2015 and 2019 were acquired as shown in Table 1. As we can see in Table 1, all the pairs have temporal

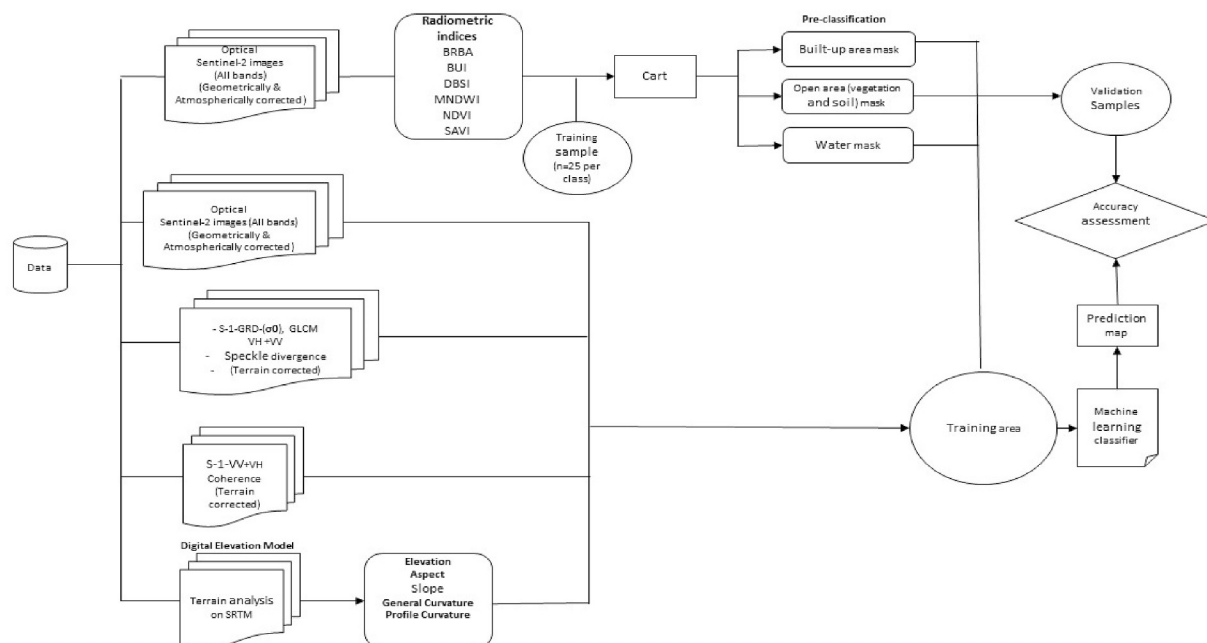


Fig. 2. Workflow of the land cover classification for the Study area.

baseline of twelve days. Furthermore, only images with the same flight direction (descending orbit) were selected to minimize the impact of topography within one investigated date.

2.3. Data processing

2.3.1. Overall study design

The overall workflow of the study is displayed in (Fig. 2.) The single components will be explained in more detail in the subsequent sections. The broad approach is shortly outlined as follows.

Six spectral indices were derived from the optical (S2) images to serve as an input to the classifier.

Radar images of (S1) and optical images of (S2) were pre-processed using SNAP (version 7.0.0) toolbox and combined to compute a large feature space for the supervised classification.

As many of the landcover classes are also dependent on the topographic conditions, a digital terrain analysis was included to provide information on landforms. The training dataset were then applied to the input features to generate a classification map for each year.

As shown in Table 1, all the optical (S2) images were acquired in the same month of the year with the SAR scenes. As a first step, radiometric calibration was applied on the Sentinel-2 images to retrieve bottom of atmosphere (BOA) surface reflectance using the sen2cor processor (version 2.5.5) (Louis et al., 2016). All bands of each single image were harmonized to a common spatial resolution of 30 m using bilinear resampling. Compared to nearest neighbor resampling, this technique alters the original pixel values and leads to a smoother-appearing image which can lead to problems in subsequent pattern recognition techniques (Lillesand and Kiefer, 2008).

The following spectral indices were computed as a feature space for the automated extraction of training areas for all investigated dates:

- Built-up Index (BUI (Lee et al., 2010; Kaimaris and Patias, 2016), equation (1)): This rather complex index makes use of the red band and the two short-wave infra-red bands (SWIR1, SWIR2) to highlight built-up surfaces for the delineation of the training areas of the urban area.
- Band Ratio for Built-up Area (BRBA (Waqar et al., 2012), equation (2)): This is an easily applied index which is used to delineate the urban area and is based on Red (R), and Short-Wave Infrared (SWIR 1).
- Normalized Difference Vegetation Index (NDVI (Rouse et al., 1973), equation (3)): This is the most frequently used vegetation index and uses the red and near infra-red (NIR) band. It highlights the vitality of vegetation based on their chlorophyll content and is used to distinguish vegetated areas.
- Soil Adjusted Vegetation Index (SAVI (Huete 1988), equation (4)): SAVI is a modification of the NDVI to correct for the influence of soil brightness when vegetation cover is relatively low and is used to maximize the difference between soil and vegetation and is used to maximize the difference between soil and vegetation.
- Modified Normalized Difference Water Index (MNDWI (Xu 2005), equation (5)): This index is based on the ratio of green and the middle infra-red (Mid-IR) band to highlight areas which are covered by water. In this study, it is used to delineate the training areas for water.
- Dry Bare-Soil Index (DBSI (Rasul et al., 2018) equation (6)): this index is used to map bare soil in a dry climate. The proposed equation is the inverse of the Modified Normalized Difference Water Index, which is based on the ratio between the difference of the reflectance in Short-Wave Infrared (SWIR1) and green band.

$$2 * ((\text{Red} * \text{SWIR2}) - (\text{SWIR1} * \text{SWIR1})) / (\text{Red} + \text{SWIR1}) * (\text{SWIR1} + \text{SWIR2}) \quad (1)$$

$$\text{Red} / \text{SWIR1} \quad (2)$$

$$(\text{nIR} - \text{red} / \text{nIR} + \text{red}) \quad (3)$$

$$((\text{nIR} - \text{Red}) / (\text{nIR} + \text{Red} + 0.5)) * (1.5) \quad (4)$$

$$(\text{Green} - \text{mIR}) / (\text{Green} + \text{mIR}) \quad (5)$$

$$((\text{SWIR1-Green}) / (\text{SWIR1+Green})) - \text{NDVI} \quad (6)$$

2.3.2. Processing of topographic input features

Braun et al. (2019) showed that the topography played a role in the identification of classes, especially in cases where large areas were covered by homogenous classes, such as water bodies and large evergreen forest areas. Similarly (Chust et al., 2004) have demonstrated that the integration of topographic features can significantly increase the quality of land cover classifications. This was also proven in other studies and can be explained by the fact that the presence or absence of certain classes of land cover or land-use are strongly determined by elevation, slope, or aspect of surfaces (Fahsi et al., 2004; Fan; 2013). Optical and radar images underlie topographically induced radiometric distortions in terms of illumination and orientation (Hale and Rock, 2003; Small, 2011).

As shown in Fig. 1, the study area shows pronounced topographical patterns, and it's divided into three sections: The Tigris River runs through the city in a wavy way from northern to southern part and divides the city into two almost equal portions left and right bank ranging between 200 and 220 m. The second part is the alluvial deposits along both sides of the river ranging between 238 and 248 m, finally the third part left, and east bank is ranging between 292 and 304 m.

To be able to describe the landcover with respect to these topographic conditions and to enhance the feature space of the supervised classification, a digital elevation model (DEM) at a spatial resolution of 30 m of the ALOS Global Digital Surface Model (ALOS, 2020) was used to derive the following parameters: DEM slope, DEM aspect, DEM profile curvature and DEM general curvature by means of digital terrain analysis (Schillaci et al., 2015).

2.3.3. Processing of Sentinel-1 data

In this study, two SAR product types (SLC Interferometric Wide Swath (IW) and GRD) of Sentinel-1 were used.

Unlike other SAR product types that use the intensity information of the SAR signal, SLC exploits the phase information of two SAR scenes acquired at different times. Hence, SLC data was utilized to derive one of the interferometric products which is the coherence image. The coherence values range between 0 and 1. Coherence close to 1 indicates that objects remain unchanged in both SAR images. Coherence close to 0 indicates that objects have changed significantly between the two SAR acquisitions. Using the coherence image over built-up areas which exhibits high coherence values (stable objects), areas of conflict can be easily detected as the values of the coherence decrease which is an indication of a change.

GRD images (VH and VV polarization) which exploit the intensity information were also used in this study. Firstly, orbit correction was applied to each of the SAR data using precise orbit files. Those orbit files provide an accurate satellite position and velocity information. Each GRD scene was radiometrically calibrated (sigma nought). Image calibration is required where each pixel value can be causally related to the radar backscatter and it also allows for image comparison acquired at different times. Due to the inherent speckle noise of SAR data, speckle noise suppression is required. Speckle filtering (Lee sigma) with window size 5 × 5 was applied (Lee et al., 2009; Nyounguiet.al 2002). Speckle divergence technique was applied on GRD SAR data to further highlight built-up areas. The variation of structures leads to a local heterogeneity that gives urban areas an extremely specific and distinct appearance in SAR images (Esch and Roth, 2004; Stasolla and Gamba, 2008; Esch et al.,

Table 2
Distribution of labelled data.

Landcover type	Labelled data
Urban	32721
River	1389
Bare soil	12900
Agriculture	11360

2010).

Furthermore, texture analysis, Grey Level Co-occurrence Matrix (GLCM) was applied on the Sentinel-1 dual-pol data. SAR data contain textural information which can be utilized to extract different features, especially in dual-pol data which contain richer information. GLCM texture analysis involves information from neighbouring pixels, which is important to characterize the different landcover classes and it is a useful tool for improving the classification accuracy. The GLCM is a measure of the probability of occurrence of two grey levels separated by a given distance in each direction, θ (Gaballerro et al., 2020). The calculation of GLCM is as follows:

$$P(i, j) = P(i, j, d, \theta) / \sum_{i=1}^I \sum_{j=1}^J P(i, j, d, \theta) \quad (7)$$

Where $P(i, j, d, \theta)$ represents the number of co-occurrence of grey levels i and j within a moving window and the adjacent distance d , in a direction given by θ

In this study, six texture measures are selected which provide the best separability amongst the landcover classes. Those measures are the following: contrast, homogeneity, energy, mean, variance and correlation. The texture measures were calculated using an 11×11 window size with an aggregate orientation of four directions ($0^\circ, 45^\circ, 90^\circ, 135^\circ$).

To evaluate the benefits of the texture analysis in helping to discriminate the urban area from the other landcover classes, we performed a separability analysis based on the Transformed Divergence (TD) method. TD is a measure of class separability and its value ranges between 0 and 2. A value close to 2 indicates that the two landcover classes are perfectly separable and a value close to 0 indicates that there is a significant overlap between the two landcover classes and hence, they are not separable. The TD distance between two classes is given by the following equation:

$$TD = 2(1 - \exp(D_{cd}/8))$$

$$D_{cd} = \frac{1}{2} \text{tr}(V_c - V_d)(V_c^{-1} - V_d^{-1}) + \frac{1}{2} \text{tr}((V_c^{-1} - V_d^{-1})(M_c - M_d)(M_c - M_d)^T) \quad (8)$$

Where V_c, V_d are the covariance matrix of c and d classes, M_c, M_d are the mean values of c and d classes, tr is the trace function and T is the transpose.

Finally, all the layers produced were collocated to the same pixel size forming a single product that is fed into the final classifier.

2.4. Training and test data

Training data were manually collected for all four landcover classes with the aid of Sentinel-2 satellite images. In total, 58370 pixels were labelled for the four different landcover classes. For urban class which is the dominant one, 32721 pixels were labelled. On the other hand, river which is the smallest class, 9900 pixels were labelled. The labelled data were split into training and testing. 70% of the total number of labelled data were used for training the model which corresponds to 40859 pixels while the rest is used for testing which corresponds to 17511 pixels. Table 2 shows the distribution of labelled data.

2.5. Classification algorithm

In this study the Support Vector Machine (SVM) classifier is employed. SVM is a popular machine learning algorithm which is used in many pattern recognition problems in recent years (Satyanarayana

and Anuradha 2013). SVM is considered one of the most powerful classifiers which has shown to outperform well established classification methods such as Artificial Neural Network (ANN) and maximum likelihood classification (MLC) and has slowly evolved into one of the most important main stream classifier (Satyanarayana and Anuradha 2013). One of the drawbacks of ANN has been associated with over fitting and local minima problems, while MLC needs large training area and assumption that the data are normally distributed (Iman et al., 2014). SVM tries to find the optimum hyperplane between classes focusing only on the support vectors which are those data that determine the margin between the classes, hence, it requires less processing time. This technique produces accurate results for binary classification. SVM classifier can be extended to multi-class classification by utilizing a number of methods such as one against all and one against one as well as kernel functions to map non-linear data.

In this study, we implemented an SVM model for multi-class classification using the Radial Basis Function (RBF). This kernel uses two parameters: C and γ . The parameter γ is very important for the model performance as high values of γ leads to greater curvature of the decision boundary which results in more accurate separation of the classes. On the other hand, very high values can lead to over-fitting. The parameter C specifies the misclassification penalty (number of points that violate the margin). As the C value increases, the margin narrows not allowing many violations. As C values decrease, the margin widens allowing many violations. Hence, appropriate values for the both parameters should be selected for the model to perform optimally.

2.6. Classification accuracy assessment

Accuracy assessment of a classified image is an essential step. It is used as a measure to evaluate the performance of the algorithm. The most common accuracy assessment approaches used in the literature to assess a classifier (Panuju et al., 2020; Vivekananda et al., 2020; Story et al., 1986) are the overall accuracy, confusion matrix and Kappa coefficient. To determine the accuracy for individual landcover classes, producer's accuracy and user's accuracy are used. Before evaluating the quality of the classification map, a target accuracy value should be specified before performing the classification. A value that is widely used in the literature as a target is to achieve an accuracy above 85% (Foody, 2008; Brown et al., 2000; Wulder et al., 2007). An accuracy of 85% and above is viewed as the standard accessibility for thematic mapping from remotely sensed imagery (Foody, 2008).

The overall accuracy of a classified image represents the accuracy of the entire product but it does not indicate how accurately each landcover class has been classified. Producer's accuracy indicates the probability that the ground truth data of a landcover class X are correctly classified as landcover X. On the other hand, user's accuracy indicates the probability that a sample from a landcover class X (on the classified image) represents that landcover X on the ground. The confusion matrix is one of the most important techniques for assessing the performance of a classifier. The confusion matrix compares the values of the ground truth data with the predicted values. The diagonal cells indicate the total number of pixels that have been correctly classified for each landcover class. The off-diagonal values represent the number of pixels that have been incorrectly classified. Kappa coefficient is another important indicator which measures the agreement between variables.

To perform the accuracy assessment, ground truth (sample size) data were collected for each landcover class. By visually inspecting Sentinel-2 images, ground truth data collected for all the years. Sentinel-2 data are of high resolution which enables an accurate extraction of ground truth data. A stratified sampling method was used to collect ground truth data for each landcover class. The purpose of stratification is to ensure that each landcover class receives an adequate number of sample points for the accuracy assessment. Firstly, an adequate overall sample size for the area of interest has been estimated for the stratified random sampling based on the equation given by Finegold et al., 2016. That sample size

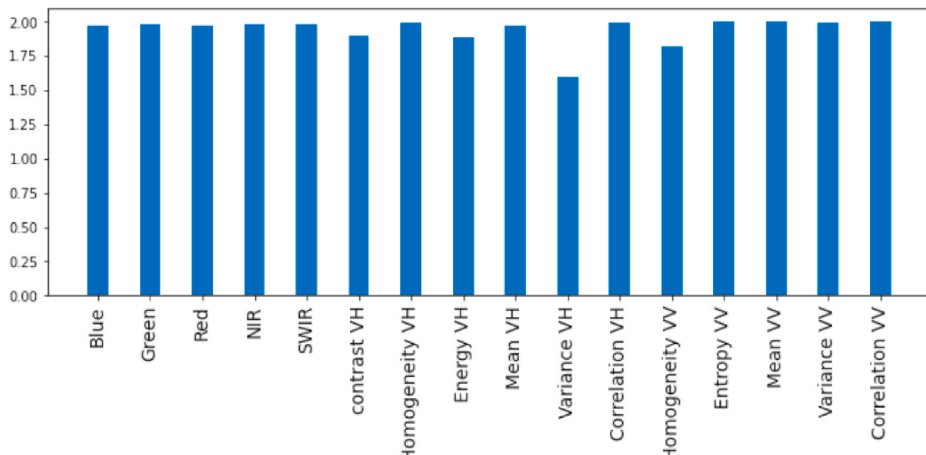


Fig. 3. Transformed Divergence separability analysis between urban and bare soil landcover class.

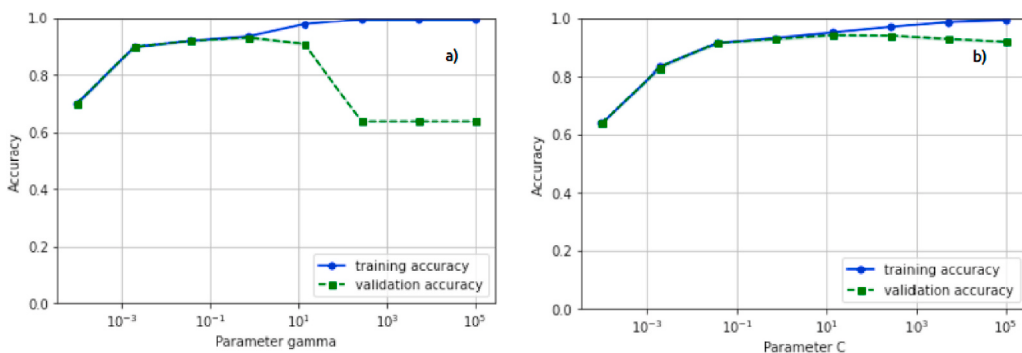


Fig. 4. Optimal parameters searching for C and γ (gamma).

has been distributed amongst the different landcover classes (strata)

$$n = (\Sigma W_i S_i / S(0))^2 \quad (9)$$

where W_i is the mapped proportion of the area of class i , S_i is the standard deviation of landcover class i and $S(0)$ is the standard error of the estimated overall accuracy.

A total of 1791 ground truth data were collected which ensures that all landcover classes on the map are adequately represented.

3. Results and discussion

3.1. Classification results

The challenge in this study was the discrimination mainly between two landcover classes: urban and bare soil. Texture analysis (GLCM) assisted in extracting the urban class and hence improve its separation from the bare soil class. GLCM proved to be an effective method in improving the spectral separability amongst different land-cover types. To assess the importance of texture analysis in landcover class discrimination, separability analysis (between the urban and bare soil landcover class) was performed, and the results are presented in Fig. 3.

The first five features in the graph corresponds to Sentinel-2 bands and the rest features corresponds to GLCM bands derived from the Sentinel-1 data. It is obvious that the Sentinel-2 bands provide very good separability between the two classes with values ranging between 1.8 and 1.9. On the other hand, looking at the performance of GLCM bands, we can see that apart from the variance VH, the rest of the texture measures reached a value above 1.8 with the Correlation VV reaching the maximum value of 2.0. The GLCM separability results indicate that they can assist in discriminating the landcover classes more accurately.

A technique called validation curve has been employed for testing different values for the hyperparameters so that the model can avoid overfitting. Overfitting is caused when the model learns the noise in the training dataset and is unable to generalize. Hence, grid search and a 10-fold cross validation was used to determine the optimal values for the two parameters. The values for C and γ parameters were tested in the range of 10^{-4} and 10^5 as shown in Fig. 4.

As it can be seen from the graphs, an incredibly low value for either γ or C parameter causes the model to underfit the data and it performs poorly. On the other hand, remarkably high values for both parameters can cause an overfitting as illustrated in the figure above. It can be seen that as both parameters become larger, the training and validation accuracy start to diverge. The training accuracy achieves an extremely high score while the validating accuracy plummets. This indicates an overfitting problem. Hence, the optimum values for C and γ are selected to be 100 and 0.4 respectively.

With the proposed method, the classification results for Mosul city (for the years between 2015 and 2019) are shown in Fig. 4A. The four land-cover classes of the map consist of urban area, agriculture, bare soil and river.

3.2. Accuracy assessment

The overall performance of SVM classifier (visually) is very good. Apart from visual inspection, accuracy indicators are used to assess the model performance as shown in Table 3 and Table 4. Information on the allocation of the sample size to each stratum is given in Table 5. Fig. 5 shows the distribution of stratified sampling points on the map.

As shown in Table 3, the overall performance of the SVM classifier is satisfactory exceeding the target accuracy. Our current methodology

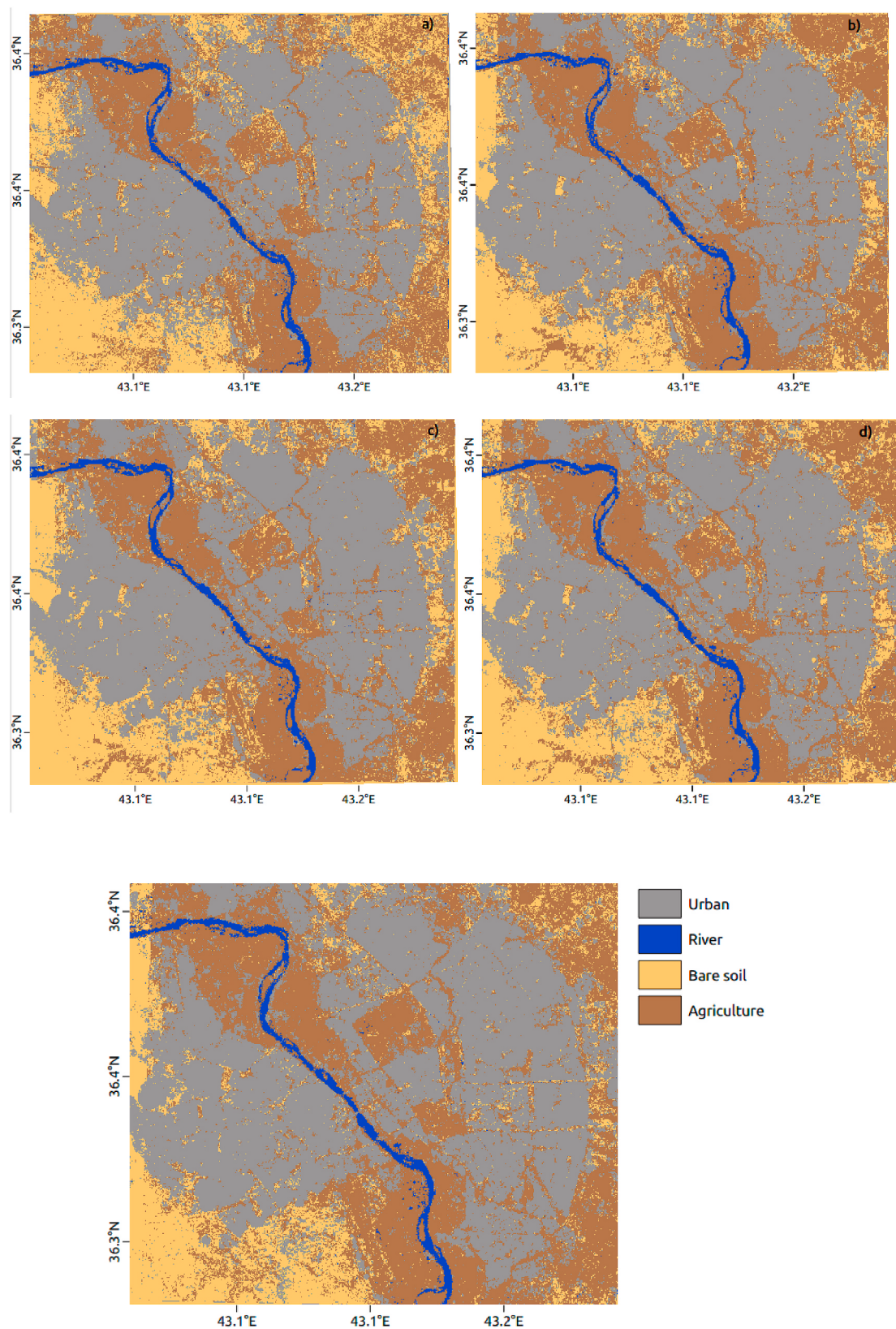


Fig. 4A. Supervised classification of time series images. a) image classification of 2015, b) image classification of 2016 c) image classification of 2017, d) image classification of 2018 and e) image classification of 2019.

Table 3
Kappa coefficient and overall accuracy of the SVM classifier.

Model performance - 2015		Model performance - 2016	
Matrices	SVM	Matrices	SVM
Overall Accuracy (%)	94.1	Overall Accuracy (%)	94.2
Kappa coefficient (%)	92.2	Kappa coefficient (%)	92.1
Model performance - 2017		Model performance - 2018	
Matrices	SVM	Matrices	SVM
Overall Accuracy (%)	94.1	Overall Accuracy (%)	94.1
Kappa coefficient (%)	92.2	Kappa coefficient (%)	91.3
Model performance - 2019			
Matrices	SVM		
Overall Accuracy (%)	94.2		
Kappa coefficient (%)	91.3		

reached an overall accuracy slightly above 94% for all classified maps and the kappa coefficient being at 92%.

Similar studies conducted on urban mapping (Ban, Y et al., 2017; Kazlova, A et al., 2018; Ban, Y and Hass, J, 2017; Khan, A et al., 2020; Semenzato, A et al., 2020, Koppel, K et al., 2015) employed different machine learning algorithms (Neural Network, KNN and SVM) with varying accuracies. Ban and Hass (2017) used an object based SVM classification on Sentinel-1 and Snetinel-2 data for mapping the urban environment of Zürich reporting an overall accuracy of 80%. Semenzato et al., 2020 employed two different algorithms (Random Forest and Maximum Likelihood) on SAR interferometric coherence data. Maximum Likelihood algorithm performed slightly better achieving an accuracy of 88%. Koppel et al., 2015 used three different methods (Difference between local area mean and local area median - referred as NM, Speckle divergence, and interferometric coherence) on Sentinel-1 data to extract the urban environment. The NM approach achieved the highest accuracy of 92%.

Looking at the confusion matrix (Table 4) we can see that the urban

class has been classified very accurately with only a few misclassified urban pixel values that have been assigned to either bare soil or agriculture landcover class. This can be attributed to the fact that the energy reflected from bare soil (in both SAR and optical imagery) is comparable with the one reflected from man-made structures. Hence, the pixels corresponding to the bare soil are mistakenly assigned to the urban class by the algorithm. We can also see some overlap in values between built up and agriculture landcover class. The reason for this is that the texture of agriculture can be similar with the one of the urban. Hence, sometimes, the reflectance values of the agriculture class can reach those values of the urban class.

In general, it is impossible to perfectly discriminate the urban from the bare soil or agriculture landcover class. The proposed methodology produced satisfactory results discriminating the two landcover classes.

3.3. Changes between 2015 and 2019

Applying the post classification change detection on the time-series classified images, a change detection map was derived showing the changes of the urban environment over time (between 2015 and 2019). Fig. 5A illustrates the changes occurred in the city of Mosul (either negative or positive) between 2015 and 2019.

Table 5

Distribution of sample size to strata. Wi is the mapped area proportion and Si is the standard deviation of the strata.

Strata	Wi	Si	Allocation
Urban	0.45	0.32	856
River	0.02	0.28	44
Agriculture	0.3	0.18	366
Bare soil	0.23	0.29	523

Table 4
Confusion matrix of the time-series data.

Confusion Matrix - 2015						
	Urban	River	Agriculture	Bare soil	User's Accuracy (%)	Producer's Accuracy (%)
Urban	851	0	2	3	99.4	99.5
River	0	43	1	0	97.8	100
Agriculture	3	0	501	19	95.5	93.4
Bare soil	0	0	54	312	85.3	89.7
Confusion Matrix - 2016						
	Urban	River	Agriculture	Bare soil	User's Accuracy (%)	Producer's Accuracy (%)
Urban	853	0	2	1	99.6	99.4
River	0	43	1	0	97.8	97.7
Agriculture	3	1	502	17	95.8	94.4
Bare soil	2	0	57	307	83.8	89.3
Confusion Matrix - 2017						
	Urban	River	Agriculture	Bare soil	User's Accuracy (%)	Producer's Accuracy (%)
Urban	852	0	3	1	99.5	99.4
River	0	43	1	0	97.8	97.8
Agriculture	3	1	504	15	96.3	94.9
Bare soil	2	0	61	303	83.7	88.8
Confusion Matrix - 2018						
	Urban	River	Agriculture	Bare soil	User's Accuracy (%)	Producer's Accuracy (%)
Urban	852	0	3	1	99.2	99.1
River	0	43	1	0	97.8	97.8
Agriculture	4	1	501	17	95.2	94.2
Bare soil	3	0	67	296	80.8	87.5
Confusion Matrix - 2019						
	Urban	River	Agriculture	Bare soil	User's Accuracy (%)	Producer's Accuracy (%)
Urban	853	0	2	1	99.2	99
River	0	41	1	0	97.9	97.9
Agriculture	4	1	503	15	96.1	86.5
Bare soil	4	0	65	297	80.4	94.2

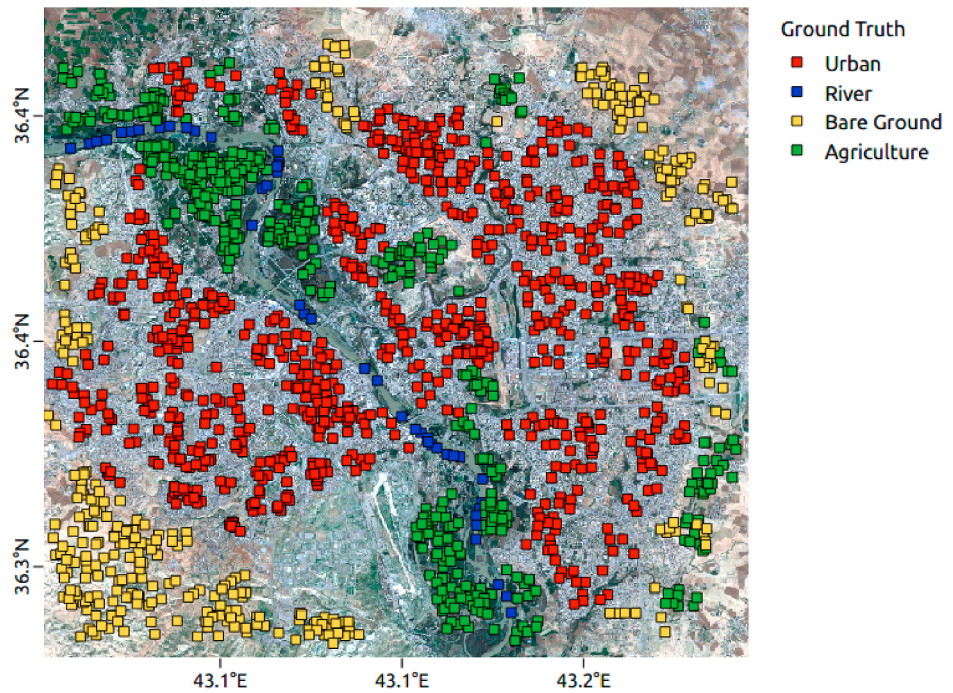


Fig. 5. Allocation of ground truth data for each class using stratified sampling.

The city of Mosul has experienced a lot of damage during the war period. The period between 2016 and 2017, apart from residential buildings, a significant number of public buildings were severely damaged as well as roads and factories. Roads and bridges were also a target and have been destroyed as it can be seen on the map in Fig. 5A.

Looking at the change detection maps, we see that Mosul city suffered the greatest destruction with the biggest settlement loss occurred the year between 2017 and 2018 shown in red. Many parts of the city have been affected, but the South West part is the most heavily damaged. In that year, many public buildings were damaged including the Mosul's airport located on the South West of the city. The reason for this is that despite the coalition's operations to liberate the city from the Islamic State (ISIS) was ended in July 2017, heavy clashes continued of ISIS resistance in the Old City resulting in devastating results. It is estimated that the city has around eight million tons of conflict debris which is equivalent to three times the Great Pyramid of Giza ([UN-Habitat and UNESCO 2018, 2019](#)). Analysis of the change detection map in Fig. 6 reveals an urban loss of over 400 km² only for the period between 2017 and 2018. On the other hand, the losses of urban area are the smallest for the period between 2016 and 2017 and from 2018 to 2019 with an urban loss close to 300 km².

In Mosul city, apart from urban losses due to war, we can also observe some positive change in some parts of the city. Efforts have been made to rebuild parts of the Mosul city during the war. The majority of positive change occurred in the period between 2018 and 2019. This is because the battlefronts between Iraqi forces and the ISIS had quieted during 2019. Agriculture and bare lands were converted to build up areas. This can be clearly illustrated in Fig. 7.

The positive change in many parts of the city is evident as shown in green colour on the map. We are focused on three main areas on the map where building re-construction was the most significant. We compare an image of 2018 with an image of 2019. In Fig. 7a we can observe the sparse buildings (top) in 2018 image compared to 2019 image (below) where the urban area looks much denser. Also, agriculture areas shown in 2018 image converted into urban the following year (Fig. 7b and c).

The devastated results in the city of Mosul due to war between 2015 and 2019 can be seen in Fig. 8. As we move from 2015 to 2019, the urban loss becomes progressively larger reaching a total urban loss of

over 1200 km² (Fig. 9). This indicates the devastated results of the war during these four years in Mosul city.

4. Conclusion

The present study presented a methodology for detecting the urban loss in the city of Mosul based on the SVM classifier and the post-classification change detection technique. The SVM classifier demonstrated that can effectively discriminate the urban area from the other landcover classes such as bare soil and agriculture which is a challenging task.

The use of microwaves (S1) alongside with the optical (S2) data enhanced the ability of the algorithm to accurately map the urban area. Furthermore, radar images can increase the quality of land cover classifications because they measure physical surface characteristics instead of spectral reflectance. This makes them especially valuable in areas of high rubble cover where urban area and debris have similar spectral characteristics. Furthermore, texture analysis proved to be useful in capturing the texture of the build-up area and enhancing the separability between landcover classes which further improved the classification results.

The results demonstrated the capability of combining both Sentinel-1 and Sentinel-2 data for mapping the built-up area very accurately. The post classification method accurately detected both negative and positive changes in Mosul's city throughout a period of five years. It was found that the largest destruction occurred between 2017 and 2018 where buildings were destroyed in many parts of the city. In 2019, it is the period where we saw most of the positive change.

Authors statement

Both authors Falah Fakhri and Ioannis Gkanatsios have participated equally in all stages of preparing and implementing of this research work.

Author contributions

F.F., and I. G.; have participated equally in this work.

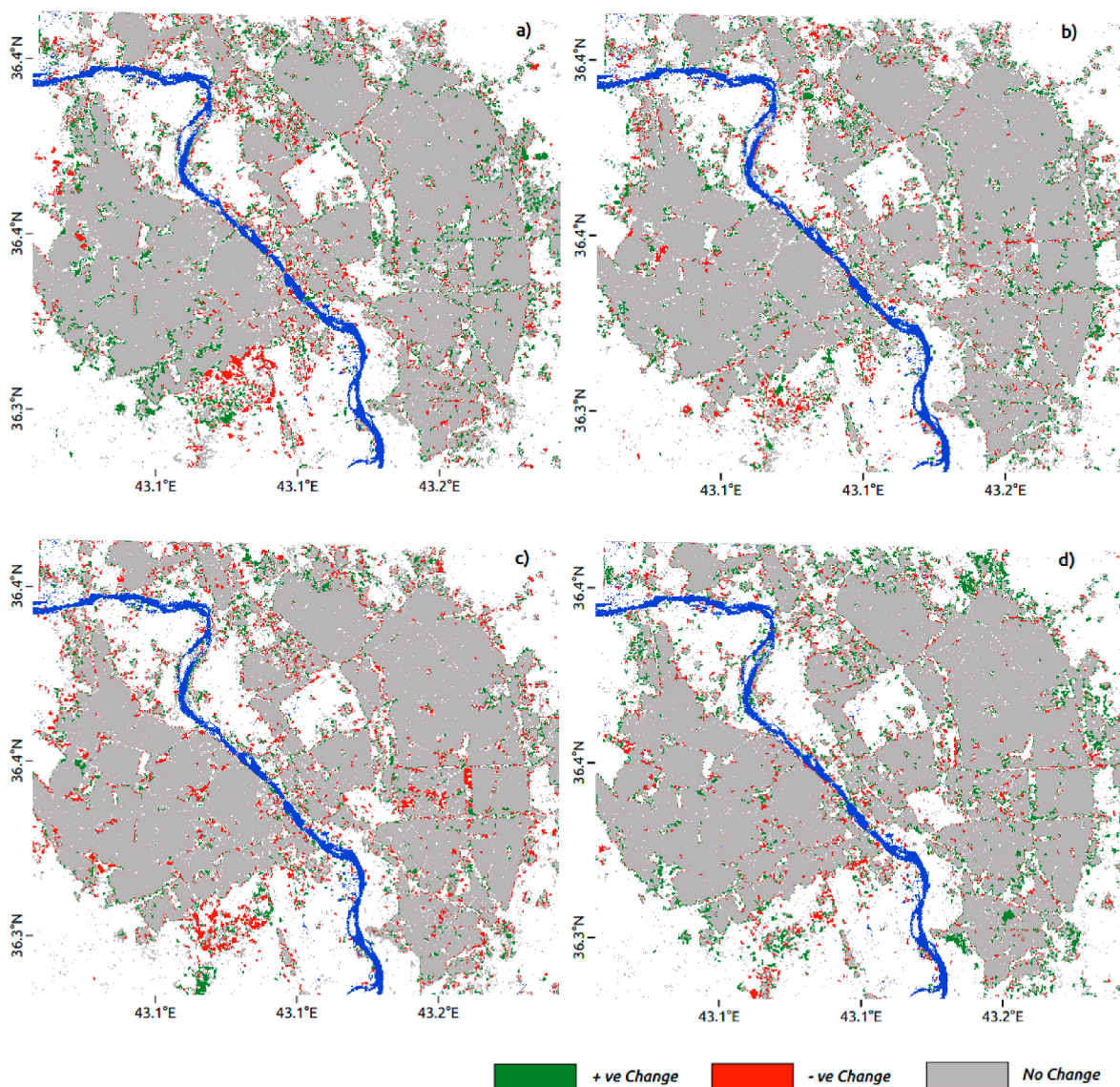


Fig. 5A. Changes in the urban environment, a) changes between 2015 and 2016, b) changes between 2016 and 2017, c) changes between 2017 and 2018, d) changes between 2018 and 2019.

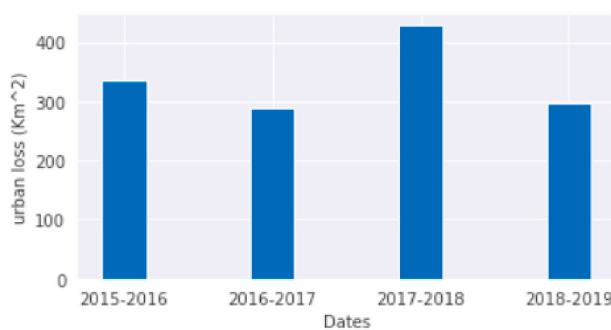


Fig. 6. Urban loss in Mosul city for each year between 2015 and 2019.

Funding

This research received no external funding.

Conflicts of interest

The authors declare no conflict of interest.

Ethical Statement for solid state ionics

- 1) This material is the authors' own original work, which has not been previously published elsewhere.
- 2) The paper is not currently being considered for publication elsewhere.
- 3) The paper reflects the authors' own research and analysis in a truthful and complete manner.
- 4) The paper properly credits the meaningful contributions of co-authors and co-researchers.
- 5) The results are appropriately placed in the context of prior and existing research.

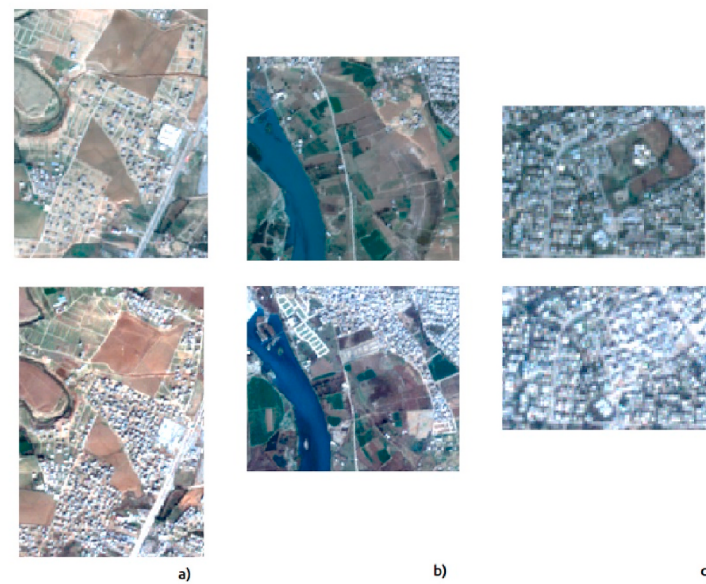
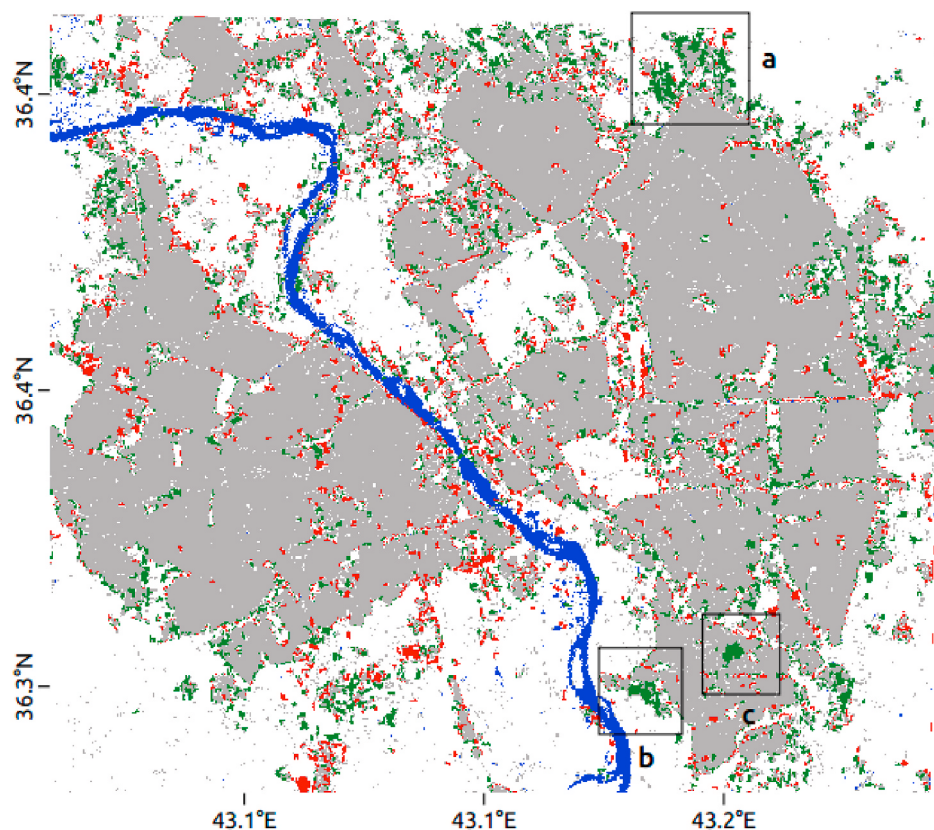


Fig. 7. Parts of Mosul's city of positive change between 2018 and 2019. Black rectangular shapes on the map show the areas where positive change occurred.

- 6) All sources used are properly disclosed (correct citation). Literally copying of text must be indicated as such by using quotation marks and giving proper reference.
- 7) All authors have been personally and actively involved in substantial work leading to the paper, and will take public responsibility for its content.

The violation of the Ethical Statement rules may result in severe

consequences.

To verify originality, your article may be checked by the originality detection software iThenticate. See also <http://www.elsevier.com/editors/plagdetect>.

CRediT authorship contribution statement

Falah Fakhri: Conceptualization, Methodology, Investigation,

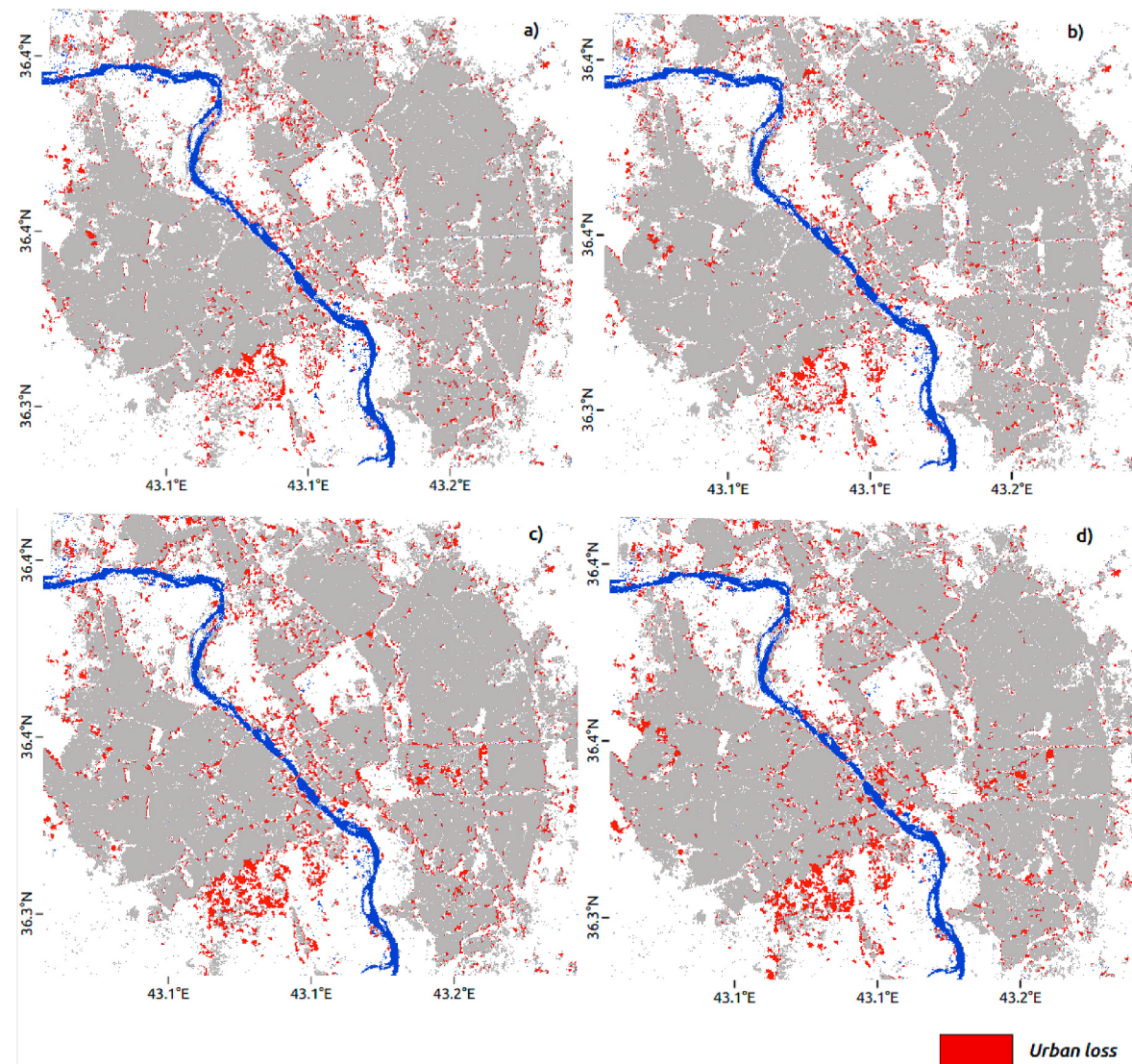


Fig. 8. Urban loss for the city of Mosul from 2015 to 2019.

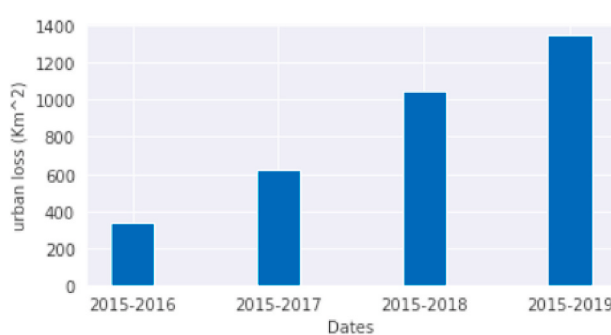


Fig. 9. Cumulative urban loss from 2015 to 2019.

Resources, Data curation, Writing – original draft, Writing – review & editing, Visualization, Writing – review & editing, Project administration. **Ioannis Gkanatsios:** Software, Validation, Formal analysis, Investigation, Resources, Data curation, Writing – original draft, Writing – review & editing, Visualization, Writing – review & editing, Project administration.

Declaration of competing interest

The authors declare that they have no known competing financial interests or personal relationships that could have appeared to influence the work reported in this paper.

References

- Afify, H.A., 2011. Evaluation of change detection techniques for monitoring land-cover changes: a case study in new Burg El-Arab area. *Alexandria Engineering Journal* 50 (2), 187–195.
- Alos Global Digital, April 2020. Surface model (DSM) ALOS world 3D-30m (AW3D30) version 3.1 JAXA EORC Japan aerospace exploration agency, Earth observation research centre. <https://www.eorc.jaxa.jp/ALOS/en/aw3d30/index.htm>.
- Ban, Y., Hass, J., 2017. Sentinel-1A SAR and Sentinel-2A MSI data fusion for urban ecosystem service mapping. *Remote Sensing Applications: Society and Environment* 8, 41–53.
- Ban, Y., Webber, L., Gamba, P., Paganini, M., 2017. EO4Urban: Sentinel-1A SAR and Sentinel-2A MSI Data for Global Urban Services. *IEEE*.
- Braun, A., Hochschild, V. Combined use of SAR and optical data for environmental assessments around refugee camps in semiarid landscapes. *ISPRS - International Archives of the Photogrammetry, Remote Sensing and Spatial Information Sciences* 2015, XL-7/W3, 777–782. doi:10.5194/isprarchives-XL-7-W3-777-2015.
- Braun, A., Fakhri, F., Hochschild, V., 2019. Refugee camp monitoring and environmental change assessment of kutupalong, Bangladesh, based on radar imagery of sentinel-1 and ALOS-2. *Rem. Sens.* 11, 2047. <https://doi.org/10.3390/rs11172047>. www.mdpicom/journal/remotesensing.

- Brown, M.H., Lewis, G., Gunn, S.R., 2000. Linear spectral mixture models and support vector machines for remote sensing. *IEEE Trans. Geosci. Rem. Sens.* 38 (5), 2346–2360.
- Chust, G., Ducrot, D., Pretus, J.L., 2004. Land cover mapping with patch-derived landscape indices. *Landsc. Urban Plann.* 69, 437–449. *Remote Sensing*, 2018, 10, pp. 1–22.
- Danish Demining Group, 2019. Hidden bombs and eight million tonnes of rubble keep the people of Mosul from returning home. <https://reliefweb.int/report/iraq/hidden-bombs-and-eight-million-tonnes-rubble-keep-people-mosul-returning-home>.
- Derakhshan, S., Cutter, S., Wang, C., 2020. Remote sensing derived indices for tracking urban land surface change in case of earthquake recovery. *Rem. Sens.* 12 (5), 895.
- El-Hattab, M.M., 2016. Applying post classification change detection technique to monitor an Egyptian coastal zone (Abu Qir Bay). *The Egyptian Journal of Remote Sensing and Space Science* 19, 23–36.
- Esch, T., Roth, A., 2004. Semi-automated classification of urban areas by means of high-resolution radar data. In: Proc. ISPRS Congr., pp. 478–482.
- Esch, T., Thiel, M., Schenck, A., Roth, A., Müller, A., Dech, S., 2010. Delineation of urban footprints from TerraSAR-X data by analysing speckle characteristics and intensity information. *IEEE Trans. Geosci. Rem. Sens.* 48 (2), 905–916.
- Fahnestock, M., Scambos, T., Moon, T., Gardner, A., Haran, T., Klinger, M., 2016. Rapid large-area mapping of ice flow using Landsat 8. *Remote Sens. Environ.* 185, 84–94.
- Fahsi, A., Tsegaye, T., Tadesse, W., Coleman, T., 2000. Incorporation of digital elevation models with Landsat-TM data to improve land cover classification accuracy. *For. Ecol. Manag.* 128, 57–64.
- Fan, H., 2013. Land-cover mapping in the Nujiang Grand Canyon: integrating spectral, textural, and topographic data in a random forest classifier. *Int. J. Rem. Sens.* 34, 7545–7567.
- Finegold, Y., Ortmann, O., Lindquist, E., d'Annunzio, R., Sandker, M., 2016. Map Accuracy Assessment and Area Estimation: A Practical Guide. Food and Agriculture Organization of the United Nations.
- Foody, G.M., 2008. Harshness in image classification accuracy assessment. *Int. J. Rem. Sens.* 11 (29), 3137–3158.
- Fung, T., LeDrew, E., 1987. Application of principal components analysis to change detection. *Photogramm. Eng. Rem. Sens.* 53 (12), 1649–1658.
- Gaballerro, R.G., Platzeck, G., Pezzola, A., Casella, A., Winschel, C., Silva, S.S., Luduena, E., Pasqualotto, N., Delegido, J., 2020. Assessment of multi-date sentinel-1 polarizations and GLCM texture features capacity for onion and sunflower classification in an irrigated valley: an object level approach, 10 (6).
- Gillanders, S.N., Coops, N.C., Wulder, M.A., Gergel, S.E., Nelson, T., 2008. Multitemporal remote sensing of landscape dynamics and pattern change: describing natural and anthropogenic trends. *Prog. Phys. Geogr.* 32, 503–528.
- Hale, S.R., Rock, B.N., 2003. Impact of topographic normalization on land-cover classification accuracy. *Photogramm. Eng. Rem. Sens.* 69, 785–791.
- Hansen, M.C., Roy, D.P., Lindquist, E., Adusei, B., Justice, C.O., Altstatt, A., 2008. A method for integrating MODIS and Landsat data for systematic monitoring of forest cover and change in the Congo Basin. *Rem. Sens. Environ.* 112, 2495–2513.
- Hue, UN-Habitat, UNESCO, 2019. The initial planning framework for the reconstruction of Mosul. UNOHABITAT, January Mosul. https://unhabitat.org/sites/default/files/documents/2019-09/initial_planning_framework_mosul_update.pdf.
- Huete, A.R., 1988. A soil-adjusted vegetation index (SAVI). *Rem. Sens. Environ.* 25, 295–309.
- Iman, N., Bahari, S., Ahmad, A., Aboobaider, M.B., 2014. Application of support vector machine for classification of multispectral data. *IOP Conf. Ser. Earth Environ. Sci.* 20 012038 20, 12038.
- Kaimaris, D., Patias, P., 2016. Identification and area measurement of the built-up area with the built-up index (BUI). Cloud publications. *International Journal of Advanced Remote Sensing and GIS* 5 (6).
- Khan, A., Govil, H., Kumar, G., Dave, R., 2020. Synergistic use of Sentinel-1 and Sentinel-2 for improved LULC mapping with special reference to bad land class: a case study for Yamuna River floodplain, India. *Spatial Information Research* 6 (28).
- Koppel, K., Zalite, K., Sisas, A., Voornmansik, V., Praks, J., Noorma, M., 2015. Sentinel for Urban Area Monitoring – Analysing Local Area Statistics and Interferometric Coherence Methods for Buildings Detection. *IEEE*.
- Kozlova, A., Khyzhniak, A., Piestova, O.I., 2018. Synergetic Use of Sentinel-1 and Sentinel-2 Data for Analysis of Urban, Development and Green Spaces, Remote Sensing Applications. *Society and Environment*.
- Lang, S., Füreder, P., Kranz, O., Card, B., Roberts, S., 2015. Papp, A. Humanitarian emergencies: causes, traits and impacts as observed by remote sensing. *Remote Sens. Handb.* 3, 483–512.
- Lee, J.S., Wen, J.H., Ainsworth, T.L., et al., 2009. Improved Sigma filter for speckle filtering of SAR imagery. *IEEE Trans. Geosci. Rem. Sens.* 47 (1), 202–213.
- Lee, J., Lee, S.S., Chi, K.H., 2010. Development of an urban classification method using a built-up index. In: Proceedings of the 6th WSEAS International Conference on Remote Sensing, Iwate, Japan, 4–6 October 2010. Iwate Prefectural University.
- Lefebvre, A., Sannier, C., Corpetti, T., 2016. Monitoring urban areas with sentinel-2A data: application to the update of the copernicus high resolution layer imperviousness degree. *Remote Sens.* 2016 8, 606. <https://doi.org/10.3390/rs8070606> mdpi.com/journal/remotesensing.
- Lillesand, T.M., Kiefer, R.W., Chipman, J.W., 2008. In: *Remote Sensing and Image Interpretation*, sixth ed. Wiley, Hoboken, NJ, USA, ISBN 9780470052457.
- Louis, J., Debaecker, V., Pflug, B., Main-Knorn, M., Bieniarz, J., Mueller-Wilm, U., Cadau, E., Gascon, F., 2016. Sentinel-2 SEN2COR. In: Proceedings of the 2016 European Space Agency Living Planet Symposium, ESA Living Planet, Prague, Czech Republic, 9–13 May, pp. 9–13.
- Ma, L., Li, M., Blaschke, T., Ma, X., Tiede, D., 2016. Object-based change detection in urban areas: the effects of segmentation strategy, scale, and feature space on unsupervised methods. *Rem. Sens.* 8, 761. <https://doi.org/10.3390/rs8090761> (www.mdpi.com/journal/remotesensing).
- Niculescu, S., Billey, A., Talab-Ou-Ali, H., 9 October 2018. Random forest classification using Sentinel-1 and Sentinel-2 series for vegetation monitoring in the Pays de Brest (France). In: Proc. SPIE 10783, Remote Sensing for Agriculture, Ecosystems, and Hydrology XX, 1078305. <https://doi.org/10.1117/12.2325546>.
- Nyoungui, N.A., Tonye, E., Akono, A., 2002. Evaluation of speckle filtering and texture analysis methods for land cover classification from SAR images. *Int. J. Rem. Sens.* 9 (23), 1895–1925.
- Pan, Z., Hu, Y., Wang, G., 2019. Detection of short-term urban land use changes by combining SAR time series images and spectral angle mapping. *Front. Earth Sci.* 1–15.
- Panuju, R.D., Paull, J.D., Griffin, L.A., 2020. Change detection techniques based on multispectral images for investigating land cover dynamics. *Rem. Sens.* 12 (11), 1781. <https://doi.org/10.3390/rs12111781>.
- Parker, N., Coles, I., Salman, R., 2014. Special Report: how Mosul fell: an Iraqi general disputes Baghdad's story. Reuters. <https://www.reuters.com/article/us-mideast-crisis-gharawi-special-report/special-report-how-mosul-fell-an-iraqi-general-disputes-baghdads-story-idUSKCN0I30Z820141014>.
- Pilon, P.G., Howarth, P.J., Bullock, R.A., Adeniyi, P.O., 1988. An enhanced classification approach to change detection in semi-arid environments. *Photogramm. Eng. Rem. Sens.* 54 (12), 1709–1716.
- Quinn, J.A., Nyhan, M.M., Navarro, C., Coluccia, D., Bromley, L., Luengo-Oroz, M., 2018. Humanitarian applications of machine learning with remote-sensing data: review and case study in refugee settlement mapping. *Phil. Trans. R. Soc. A376*, 20170363. <https://doi.org/10.1098/rsta.2017.0363>.
- Radke, R.J., Andra, S., Al-Kofahi, O., Roysam, B., March 2005. Image change detection algorithms: a systematic survey. In: *IEEE Transactions on Image Processing*, vol. 14, pp. 294–307, 3.
- Rasul, A., Balzter, H., Ibrahim, F.G.R., Hameed, H.M., Wheeler, J., Adamu, B., Ibrahim, S., Najmaddin, P.M., 2018. Applying built-up and bare-soil indices from Landsat 8 to cities in dry climates. *Land* 7, 81. <https://doi.org/10.3390/land703008>. <https://www.mdpi.com/journal/land>.
- Revkin, M., Jebari, D., 2019. West Mosul perceptions on return and reintegration among stayees, IDPs and returnees. International Organization for Migration (IOM). www.iom-miraq.net.
- Rouse, J.W., Haas, R.H., Schell, J.A., Deering, D.W., 1973. Monitoring the Vernal Advancement and Retrogradation (Green Wave Effect) of Natural Vegetation. Type II Report for Period September 1973–March 1973.
- Satyana Rayana, C.H., Anuradha, S., 2013. A review of recent texture classification methods. *IOSR J. Comput. Eng.* 14 (1), 54–60.
- Schillaci, C., Braun, A., Kropáček, J., 2015. 2.4.2. Terrain analysis and landform recognition. *Geomorphol. Tech.* 2, 1–18.
- Semenzato, A., Pappalardo, E.S., Codato, D., Trivelloni, U., De Zorzi, S., Ferrari, S., De Marchi, M., Massironi, M., 2020. Mapping and monitoring urban environment through sentinel-1 SAR data: a case study in the veneto region (Italy). *ISPRS Int. J. Geo-Inf.* 6 (9).
- Hayet Si Salah, Samy Ait-Aoudia, Abdelmounaam Rezgui & Sally E. Goldin, Change detection in urban areas from remote sensing data: a multidimensional classification scheme, *Int. J. Rem. Sens.*, 40:17, 6635–6679, DOI: 10.1080/01431161.2019.1583394.
- Small, D., 2011. Flattening gamma: radiometric terrain correction for SAR imagery. *IEEE Trans. Geosci. Rem. Sens.* 49, 3081–3093.
- SNAP - ESA Sentinel application platform v2.0.2, <http://step.esa.int>.
- Stasolla, M., Gamba, P., Jun, 2008. Spatial indexes for the extraction of formal and informal human settlements from high-resolution SAR images. *IEEE J. Sel. Topics Appl. Earth Obs. Remote Sens.* 1 (2), 98–106.
- Story, M., Goncalon, G.R., 1986. Accuracy assessment: a user's perspective. *Photogramm. Eng. Rem. Sens.*
- Stow, D.A., Lippitt, C.D., Coulter, L.L., Davis, B.A., 2015. Time-sensitive remote sensing systems for post-hazard damage assessment. In: Lippitt, C.D., Stow, D.A., Coulter, L. L. (Eds.), *Time-Sensitive Remote Sensing*, vols. 13–28. Springer, New York, NY, USA, ISBN 978-1-4939-2601-5.
- Suriyaprasit, M., Shrestha, D.P., 2008. Deriving land use and canopy cover factor from remote sensing and field data in inaccessible mountainous terrain for use in soil erosion modelling. *Int. Arch. Photogram. Rem. Sens. Spatial Inf. Sci.* 42, 1747–1750.
- Tapete, D., Donoghue, D., Cigna, F., Phili, G., 2015. Mapping changes and damages in areas of conflict: from archive C-band SAR data to new HR X-band imagery, towards the Sentinels. In: Proc. 'Fringe 2015 Workshop', Italy, Frascati.
- Tavares, P.A., Santos Beltrão, N.A., Guimarães, U.S., Teodoro, A.C., 2019. Integration of sentinel-1 and sentinel-2 for classification and LULC mapping in the urban area of belém, eastern Brazilian amazon. *Sensors* 19, 1140. <https://doi.org/10.3390/s19051140> mdpi.com/journal/sensors.
- Van Westen, C.J., 2013. Remote sensing and GIS for natural hazards assessment and disaster risk management. *Treatise Geomorphol.* 3, 259–298.
- Verbesselt, J., Hyndman, R., Newham, G., Culvenor, D., 2010. Detecting trend and seasonal changes in satellite image time series. *Remote Sens. Environ.* 114, 106–115.
- Vivekananda, G.N., Swathi, R., Sujith, A., 2020. Multi-temporal image analysis for LULC classification and change detection. *European journal of remote sensing* 54, 189–199. <https://doi.org/10.1080/22797254.2020.1771215>. <https://www.tandfonline.com/doi/full/10.1080/22797254.2020.1771215>.
- Waqr, M.W., Mirza, J.F., Mumtaz, F., Hussain, E., 2012. Development of new indices for extraction of built-up area & bare soil from Landsat data. *Open Access Scientific Reports* 1 (Issue 1). <http://www.omicsonline.org/scientific-reports.php>. Digital Object Identifier. <https://doi.org/10.4172/scientificreports.136>.

- Washaya, P., Balz, T., Mohamadi, B., 2018a. Coherence change-detection with sentinel-1 for natural and anthropogenic disaster monitoring in urban areas. *Rem. Sens.* 10, 1026. <https://doi.org/10.3390/rs10071026>. <https://www.mdpi.com/journal/remotesensing>.
- Washaya, P., Balz, T., Mohamadi, B., 2018b. Coherence change-detection with sentinel-1 for natural and anthropogenic disaster monitoring in urban areas. *Rem. Sens.* 10 (7), 1–22.
- Wulder, A.M., Steven, E.F., White, J.C., Linke, J., Magnussen, S., 2006. An accuracy assessment framework for large-area land cover classification products derived from medium-resolution satellite data. *Int. J. Rem. Sens.* 27 (4), 663–683.
- Xu, H., 2005. A study on information extraction of water body with the modified normalized difference water index (MNDWI). *Journal of Remote Sensing* 9 (5), 511–517.